

*Chapter 1***EQUATION OF STATE FOR PROTO-NEUTRON STAR***G. Shen**

Theoretical Division, Los Alamos National Laboratory, Los Alamos, NM, 87545, USA

Abstract

Physics of the Equation of State (EoS) for proto-neutron star (PNS) concerns properties of neutron rich matter at finite temperature over wide range of densities. In this contribution we discuss the structure of PNS inner crust in a relativistic mean field model with spherical Wigner-Setiz approximation, and the composition of matter around neutrino-sphere in PNS in a virial expansion of non-ideal gas composed of nucleons and nuclei. We go on to discuss several new complete EoS for PNS and supernova, whose detailed composition is important for the neutrino dynamics. We focus on one important distinction for various EoS - the density dependence of symmetry energy E'_{sym} , and its interesting correlation with the radii of neutron star, as well as properties of neutron distribution in neutron rich nuclei. Improved understanding of E'_{sym} from terrestrial experiment on neutron distribution of neutron rich nuclei, benchmark calculations via ab initio methods, and statistical analysis on good quality observational data will advance our knowledge on EoS.

PACS 21.65.Mn,26.50.+x,26.60.Kp,21.60.Jz **Keywords:** Proto-Neutron Star; Equation of State of Nuclear Matter.

*E-mail gshen@lanl.gov

1. Introduction

Proto-neutron star (PNS) is born subsequent to gravitational core collapse supernova, which explodes once every second in our universe. In this chapter we describe the equation of state (EoS) of nuclear matter for PNS, particularly the structure of inner crust and composition around neutrino-sphere, which is the last scattering site before neutrinos leave PNS. The EoS is tied to many important questions in nuclear physics and astrophysics: what is the biggest and largest neutron star that nature could make? what's the role of neutrino-matter interaction in supernova explosion dynamics? what's the spectrum of neutrinos emerged from neutrino-sphere and eventually observable in future terrestrial detectors? where did the chemical elements beyond iron come from?

The EoS for hot, dense matter relates energy and pressure to temperature, density, and composition. The properties of hot dense matter, for example its pressure at high baryon density - larger than normal nuclear density 3×10^{14} g/cm³, have been the focus of many extraordinary terrestrial experiments, including heavy ion collisions with Au [1]. The pressure of nuclear matter at high density determines how large a neutron star our nature could realize.

The properties of nuclear matter depends on its composition, particularly the proton-neutron number asymmetry, or iso-spin dependence, conveniently characterized by the parameter called (a)symmetry energy E_{sym} . Most stable nuclei have a small such asymmetry and tell us little about how the EoS changes with the asymmetry. The neutron/proton rich isotopes will be studied with new tools like the Facility for Rare Isotope Beams (FRIB) [2], a heavy ion accelerator to be built in Michigan State University. Studies by these new tools will help us understand when the nuclei would become unstable upon too many neutrons (or protons) added, and ultimately tell us the composition of nuclear matter in PNS given temperature, density, and proto-neutron asymmetry.

Density dependence of symmetry energy E'_{sym} is one key unknown in nuclear physics and nuclear astrophysics, where neutron rich matter is particularly relevant. There are many interesting correlations with E'_{sym} that have been studied in recent years. The pressure of nuclear matter is proportional to E'_{sym} . With a higher pressure if E'_{sym} is large, neutron rich nucleus, such as ²⁰⁸Pb, is found to have a larger neutron radius [3]. This has motivated the Lead Radius Experiment (PREX) [4] to accurately measure the neutron radius in ²⁰⁸Pb with parity violating electron scattering [5]. On the other hand, the radius of a canonical 1.4 solar mass neutron star is determined by the nuclear matter at similar density inside ²⁰⁸Pb, therefore a larger pressure at such density tends to give a bigger radius for 1.4 solar mass neutron star [6]. Current large uncertainties in the EoS lead us to generate several big tables of EoS based on distinct properties of nuclear matter at high densities, which could be used in astrophysical simulations such as PNS evolution to identify astrophysical observables with related nuclear matter properties.

The dynamical response of nuclear matter, important for the evolution of PNS, depends on its detailed composition. In the inner crust of PNS, nuclei with unconventional shapes such as plate or rod like could appear [7]. Neutrinos could coherently scatter off these novel nuclei - nuclear pasta, because such nuclear shapes have sizes comparable to neutrino de-Broglie wavelength in PNS [8]. Moreover, light nuclei could be abundant around neutrino-sphere, therefore influence the spectra of neutrinos emerged from neutrino-sphere

[9]. Finally, the neutrino spectra from PNS determine the neutron-proton ratio in the neutrino driven wind from supernova, which is one most promising site for neutron rich nuclei to be synthesized [10].

The chapter is organized as follows. In section 2 we describe the structure of PNS inner crust in a relativistic mean field model with spherical Wigner-Seitz approximation for the lattice. In section 3 we describe the EoS around neutrino sphere in a virial expansion of nonideal gas of nucleons and nuclei. In section 4 we discuss several new complete EoS tables covering large range of densities, temperatures, and proton fractions, to be used in astrophysical simulations. In the following section 5, we discuss one important distinction among the various EoS tables, the density dependence of symmetry energy at high density and its correlation with various observables. Finally we conclude in section 6.

2. Structure of Inner Crust

Realistic calculations with modern nuclear interactions for the structure of neutron star crust started with the seminal work of Negele and Vautherin, who applied a Skyrme Hartree-Fock calculation with two-body potentials [11], and obtained the ground state within the spherical Wigner-Seitz (WS) approximation. In WS approximation, the unit cell of a crystal lattice is modeled as a sphere. They found, as the system became more neutron rich and the density increased, neutrons escaped and the system approached a uniform state near nuclear density. Since then there have been many investigations [12] with more sophisticated interactions and more complicated lattice configurations, such as rods or plates. These non-spherical ‘pasta’ phases, which seem to appear within a significant range of sub-nuclear densities are relevant for the structure of neutron star crusts [13, 14] and the dynamics of supernovae [15]. For simplicity, this contribution is limited to discuss perfect crystal with a single nuclear species at lattice sites (for the possibility of heteronuclear compounds, see Ref. [16] and references therein).

In proto-neutron star, neutrinos are trapped for tens of seconds in the hot, dense nuclear medium. The proton fraction in thermal beta equilibrium matter therefore evolves as neutrinos diffuse out of proto-neutron star. As a result, one has to consider a large range of proton fractions, as well as temperatures, in the equation of state for PNS. For hot nuclear matter, assuming that the spherical WS cell still remains a good approximation to the realistic lattice structure, people have studied the EoS with different models. Using a phenomenological compressible liquid-drop model, Lattimer and Swesty [17] (L-S) produced an equation of state for hot dense matter that has been widely used in supernova simulations. Later, H. Shen *et al.*[18] (S-S) constructed an equation of state based on Thomas-Fermi and variational approximations to a relativistic mean field (RMF) energy functional. However neither method takes into account the shell structure of finite nuclei or explores the full range of density distributions possible even in the spherical WS approximation.

In recent years, RMF models have provided a consistent description for the ground state properties of finite nuclei, both along and far away from the valley of beta stability [19, 20, 21, 22, 23]. These models incorporate the spin-orbit splitting naturally and the relativistic formalism provides a framework to extrapolate the properties of non-uniform and uniform nuclear matter to high densities. Furthermore there is a close relation between phenomenological RMF models, that simply fit parameters to properties of finite nuclei,

and more systematic effective field theory approaches that enumerate all of the possible interactions allowed by symmetries.

In this section, we use an RMF model for non-uniform matter at intermediate density (and can be easily extended to uniform matter at high density). Low density pure neutron matter is analogous to a unitary gas [26], where the neutron-neutron scattering length is much larger than both the effective range of nuclear force and the average inter-particle spacing. To better describe neutron-rich matter at low density, we use a density dependent scalar meson-nucleon coupling. At high density, the model reduces to the normal RMF parameter set NL3 [27]. The unit lattice of non-uniform nuclear matter is conveniently approximated by a spherical WS cell. The meson mean fields and nucleon Dirac wave functions inside the Wigner-Seitz cell are solved fully self-consistently. The size of the WS cell is found by minimization of the free energy per nucleon. The WS approximation provides a framework to incorporate the best known microscopic nuclear physics [11]. The nuclear shell structure effects are included automatically and it is already possible for some effects of complex nuclear pasta states to be included in spherical calculations in the form of shell states [28]. Full three-dimensional WS calculations, by various nuclear models including liquid droplet models, quantum molecular dynamic simulations, and Hartree-Fock calculations, predict a whole sequence of pasta phases [29, 7, 8], which would make the transition to uniform matter more smooth. However this will demand increased complexity and much larger computational resources if one wishes to generate complete EoS for PNS. For simplicity in this contribution we use the spherical WS approximation.

2.1. Non-uniform nuclear matter in Wigner-Seitz approximation

The formalism for relativistic mean field theory has been reviewed in previous works, see eg [21, 22, 23, 24, 28]. The basic ansatz of the RMF theory is a Lagrangian density where nucleons interact via the exchange of sigma- (σ), omega- (ω_μ), and rho- (ρ_μ) mesons, and also photons (A_μ).

$$\begin{aligned}
\mathcal{L} = & \bar{\psi}[i\gamma^\mu\partial_\mu - m - \Gamma_\sigma\sigma - g_\omega\gamma^\mu\omega_\mu \\
& - g_\rho\gamma^\mu\vec{\tau}\cdot\vec{\rho}_\mu - e\gamma^\mu\frac{1+\tau_3}{2}A_\mu]\psi \\
& + \frac{1}{2}\partial^\mu\sigma\partial_\mu\sigma - \frac{1}{2}m_\sigma^2\sigma^2 - \frac{1}{3}g_2\sigma^3 - \frac{1}{4}g_3\sigma^4 \\
& - \frac{1}{4}\omega^{\mu\nu}\omega_{\mu\nu} + \frac{1}{2}m_\omega^2\omega^\mu\omega_\mu + \frac{1}{4}c_3(\omega^\mu\omega_\mu)^2 \\
& - \frac{1}{4}\vec{\rho}^{\mu\nu}\cdot\vec{\rho}_{\mu\nu} + \frac{1}{2}m_\rho^2\vec{\rho}^\mu\cdot\vec{\rho}_\mu - \frac{1}{4}A^{\mu\nu}A_{\mu\nu}
\end{aligned} \tag{1}$$

Here the field tensors of the vector mesons and the electromagnetic field take the usual forms. To fit neutron rich matter at low density from ab initio methods, we introduce a density dependent coupling between the scalar meson and the nucleon, $\Gamma_\sigma = \Gamma_\sigma(n)$ ($n \equiv \sqrt{j_\mu j^\mu}$ is baryon density and j_μ is nucleonic current).

In charge neutral nuclear matter composed of neutrons, n , protons, p , and electrons, e , there are equal numbers of electrons and protons. Electrons can be treated as a uniform

Fermi gas at high densities ¹. They contribute to the Coulomb energy of the *npe* matter and serve as one source of the Coulomb potential in nuclear mean field.

The variational principle leads to the following equations of motion

$$[\alpha \cdot \mathbf{p} + V(\mathbf{r}) + \beta(m + S(\mathbf{r}))]\psi_{\mathbf{i}} = \varepsilon_{\mathbf{i}}\psi_{\mathbf{i}} \quad (2)$$

for the nucleon spinors, with vector and scalar potentials

$$\begin{aligned} V(\mathbf{r}) &= \beta\{g_{\omega}\omega_{\mu} + g_{\rho}\vec{\tau} \cdot \vec{p}_{\mu} + e^{\frac{(1+\tau_3)}{2}} A_{\mu} + \Sigma^R\}, \\ S(\mathbf{r}) &= \Gamma_{\sigma}\sigma, \end{aligned} \quad (3)$$

where

$$\Sigma^R = \frac{\gamma^{\mu}j_{\mu}}{n} \frac{\partial \Gamma_{\sigma}}{\partial n} \rho_s \sigma, \quad (4)$$

is the rearrangement term due to the density dependent coupling between the sigma meson and the nucleon, and ρ_s is the scalar density of nucleons. The form of Σ^R is adjusted to reproduce ab initio neutron matter calculation at low density [30].

In the WS approximation, the lattice Coulomb energy consists of contributions from neighboring unit cells. This correction to the WS Coulomb energy is important for determining the stable configuration of WS cells and the transition density to uniform matter, especially when the system has a large proton fraction. We include the exact Coulomb energy in calculating the free energy of WS cell of radius R_c . Following the treatment in Ref. [31, 32], we calculate the Coulomb energy per unit cell as,

$$W_c = \frac{1}{2} \sum'_{\vec{G}} \frac{I_{hkl}^2}{a^3 \vec{G}^2}, \quad (5)$$

where a is lattice constant defined by $a^3 = V_{cell} = \frac{4\pi}{3}R_c^3$, and

$$\vec{G} = h\vec{A} + k\vec{B} + l\vec{C}. \quad (6)$$

Here h, k , and l are integers, and \vec{A}, \vec{B} , and \vec{C} are the primitive transformation vectors of the reciprocal lattice. The prime on the sum means that the point $\vec{G} = 0$ is excluded. The form factor I_{hkl} is given by

$$I_{hkl} = \int_{cell} \rho_p(\vec{r}) e^{-i\vec{G} \cdot \vec{r}} d\vec{r}. \quad (7)$$

Oyamatsu *et al.* [32] assumed a uniform proton density inside the nucleus and found that the stable configuration is a Body-Centered Cubic (BCC) lattice. Using realistic proton density distribution, we also find that a BCC lattice gives the lowest Coulomb energy. The electron charge screening effects are negligible since the electron Thomas-Fermi screening length is larger than the lattice spacing in the inner crust [33]. There are also small corrections due to electron-exchange interactions and electron polarizations, which are discussed in Ref. [34].

In the spherical Wigner-Seitz approximation, the unit cell of a crystal lattice, complex close-packed polyhedron, is approximated by a spherical cell of the same volume. One WS

¹It needs electron density $> 10^6$ g/cm³, which is easily surmounted in the regime considered in the inner crust.

cell has one nucleus. We apply boundary conditions on the wave functions at the edge of WS unit cell. To achieve a uniform density distribution for a free neutron gas, we require that at the cell radius, all wave functions of even parity vanish, and the radial derivative of odd parity wave functions also vanishes [11].

2.2. Solutions for Wigner-Seitz cells

For nonuniform matter we find new shell states which minimize the free energy per baryon over a significant density range. Shell states have inside and outside surfaces and they can minimize the Coulomb energy of high Z (large proton number) configurations at the expense of a larger surface energy. These shell states may be related to the appearance of a central depression in the density of super heavy nuclei [35] because of their large coulomb energies. The appearance of shell states may significantly change transport properties such as the shear viscosity and shear modulus of neutron rich matter.

To determine the minimum free energy per baryon at a specified baryon density n_B , one must search over the cell radius R_c . When R_c is large and n_B is beyond the neutron drip density $\sim 10^{11}$ g/cm³ for neutron rich matter, one will need to take into account a large number of levels, since the nucleon number is $A = 4\pi R_c^3 n_B / 3$. The fact that the matter is at finite temperature will require one to consider even more levels. For example, when $n_B = 0.080$ fm⁻³, proton fraction $Y_p = 0.4$, and $R_c = 23.5$ fm, there are 4892 nucleons inside one WS cell and one needs to include 427 (419) neutron (proton) levels. It is hard to achieve self-consistency for the mean fields with a large number of levels. To ensure the convergence of the self-consistent iterations for the mean fields, it is important to have a good initial guess for the mean field potentials. Here our strategy is to employ the convergent potentials for a nucleus with a smaller R_c as the starting guess for a nucleus with a slightly larger R_c . In this way, new shell states with large cell radii are found. These can minimize the free energy over a significant density range.

We show in Fig. 1 an example of how shell states were found. Here the free energy per baryon versus WS cell radius is displayed for baryon densities of 0.040, 0.049, 0.080, and 0.090 fm⁻³ when $Y_p = 0.4$ and temperature $T = 1$ MeV. For each baryon density, there are two minima of free energy per baryon at different WS radii, denoted as open circles. The neutron and proton density distributions of the WS cells with these two radii are shown in Fig. 2. The first minimum at smaller WS cell radius corresponds to a nucleus with a normal density distribution. The second minimum at larger WS cell radius corresponds to a shell shaped density distribution. Here the nucleus has both outside and inside surfaces and the neutron and proton densities are only non-vanishing at intermediate r . We call the first minimum a nucleus state and the second minimum a shell state. For the shell state, the sum of neutron and proton densities (at intermediate radius r) is close to the saturation density of nuclear matter ~ 0.15 fm⁻³, as one expects from nuclear saturation.

At $n_B = 0.049$ fm⁻³, the two minima of free energy per baryon become degenerate, as shown in upper right panel of Fig. 1. Below 0.049 fm⁻³, the first minimum with smaller cell radius corresponding to a normal nucleus is the absolute minimum and therefore the equilibrium state (*e.g.*, panel a of Fig. 1). On the other hand, above 0.049 fm⁻³, the second minimum corresponding to a shell state is the true equilibrium state (*e.g.*, panels c and d of Fig. 1). Therefore 0.049 fm⁻³ is the critical baryon density when the density distribution

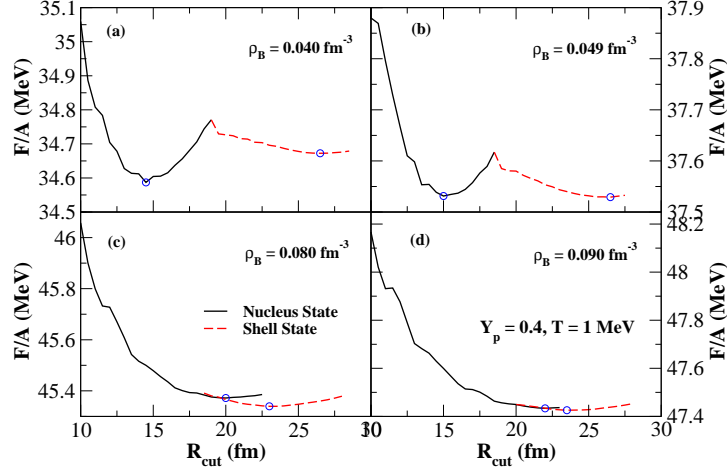


Figure 1. (Color online) Free energy per baryon versus Wigner-Seitz cell radius R_c for baryon densities of $n_B = 0.040$ (a), 0.049 (b), 0.080 (c), and 0.090 fm^{-3} (d). The proton fraction is $Y_p = 0.4$ and the temperature is $T = 1 \text{ MeV}$. The two circles denote minima for the nucleus (small R_c) and shell states (larger R_c).

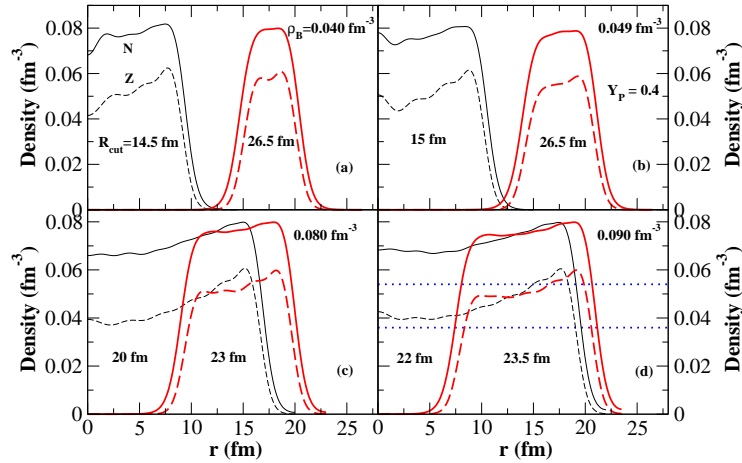


Figure 2. (Color online) The neutron (solid line) and proton (dash line) density distributions for the Wigner-Seitz cells with baryon densities of $n_B = 0.040$ (a), 0.049 (b), 0.080 (c), and 0.090 fm^{-3} (d). The proton fraction is $Y_p = 0.4$ and $T = 1 \text{ MeV}$. The red curves give density distributions for shell states. The black curves give density distributions for nucleus states. The corresponding cell radii are shown in each panel. The dotted lines in the lower right panel are neutron (upper) and proton (lower) densities for uniform matter.

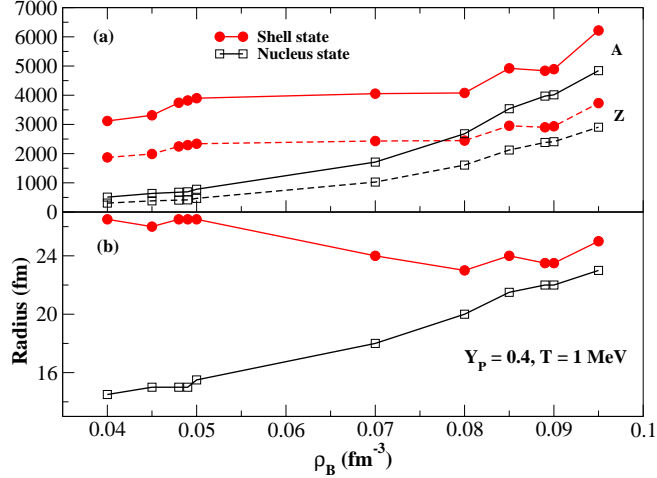


Figure 3. (Color online) The atomic and proton numbers (panel a), and the WS cell radii for nucleus (squares) and shell states (filled circles) (panel b) shown as functions of the baryon density for $Y_p = 0.4$.

inside the WS cell changes from a normal nucleus to a shell state. In the lower right panel of Fig. 2, we also show the uniform neutron and proton density distributions by dotted lines when $n_B = 0.090 \text{ fm}^{-3}$. 0.090 fm^{-3} is in fact the transition density from a shell state to uniform matter.

In Fig. 3, the corresponding atomic and proton numbers A and Z for nucleus and shell states (upper panel), and the corresponding WS cell radii (lower panel) are shown as functions of the baryon density. At low baryon densities, the WS cell radius of the shell state is about twice that of the nucleus state, *e.g.*, 26 fm vs. 14 fm at $n_B = 0.040 \text{ fm}^{-3}$. The cell radii of shell states decrease with increasing density, while those of nucleus states increase with density. They approach one another at high baryon densities: 24 fm vs. 22 fm at 0.090 fm^{-3} . For both nucleus and shell states, A and Z increase with increasing baryon density.

In this section our discussion is focused on $Y_p = 0.4$ and $T = 1 \text{ MeV}$ due to limit of space. The calculation has been extended to a large range of proton fractions and temperatures. We calculate the resulting EoS for the inner crust (and core) of PNS at over 107,000 grid points in the proton fraction range $Y_p = 0$ to 0.56 . For the temperature range $T = 0.16$ to 15.8 MeV we cover the density range $n_B = 10^4$ to 1.6 fm^{-3} ; and for the higher temperature range $T = 15.8$ to 80 MeV we cover the larger density range $n_B = 10^8$ to 1.6 fm^{-3} .

3. Composition around neutrino-sphere

Simulations of the core collapse supernovae and evolution of PNS depend heavily on the EoS at subnuclear density. Detailed information on the distributions of nuclei in the EoS table is important for neutrino-matter dynamics [36]. Neutrinos radiate 99% of the energy

released in supernovae. Besides gravitational wave signals, neutrinos are the only messenger through which one can directly probe the EoS inside supernovae. The neutrinosphere is the surface of last scattering before ν or $\bar{\nu}$ escape. The neutrinosphere is expected to be at a density around 10^{11} g/cm³ and this is consistent with the available information from a handful of events in SN1987a [37, 38]. The composition of matter at subnuclear density constrains the position of the neutrinosphere and influences the spectra of emitted neutrinos and antineutrinos. For example, in a recent study [9], light nuclei with mass 2, 3 and 4 were found to have an important influence on the spectra of electron anti-neutrinos.

Nuclear statistical equilibrium (NSE) models treat low density nuclear matter as a system of noninteracting nuclei in statistical equilibrium, taking into account the binding properties of heavy nuclei. This has been widely used in nuclear astrophysics [39]. Recently, there have been several NSE based studies of the supernova EoS, see for example Refs. [40] and [41].

In this section, we discuss subnuclear density nuclear matter in a virial expansion for a nonideal gas, consisting of neutrons, protons, alpha particles, and 8980 species of heavy nuclei ($A \geq 12$) with masses from the finite-range droplet model (FRDM) [42]. The virial results will cover the density range $n_B = 10^{-8}$ to 0.1 fm⁻³, the temperature range $T = 0.158$ to 15.8 MeV, and the proton fraction range $Y_P = 0.05$ to 0.56 . (For temperature higher than 15.8 MeV, matter is uniform and fully described in the RMF model.) The distribution of nuclei for given conditions is obtained in this approach, while the existing EoS tables of Lattimer-Swesty (L-S) [17] and H. Shen, Toki, Oyamatsu and Sumiyoshi (S-S) [18, 43], use a single heavy nucleus approximation. The virial expansion is very similar to NSE when heavy nuclei are dominant, but includes important interactions between nucleons and light nuclei. The virial expansion is exact at low density limit when light elements dominate and fugacity of nucleons is small. Our virial EoS will be matched, using a thermodynamically consistent interpolation scheme, to the RMF EoS obtained in previous section to generate full EoS table for PNS and supernova.

We include the second order virial corrections among nucleons and alphas as in Ref. [44], where the second order virial coefficients are obtained from scattering phase shift data. Partition functions for heavy nuclei are included using the recipes of Fowler *et al.* [45] (some calculations are presented using partition functions based on the recipe of Rauscher *et al.* [46] for comparison in Ref. [30] and the results are similar). Equivalently, the partition functions can be considered as the sum of successive high orders of the virial expansion for heavy nuclei. There have been many studies on the level density and partition functions of hot nuclei in astrophysical environments. For large scale astrophysical applications, it is necessary to find both reliable and computationally practical methods for the level density. Most of these studies [47, 45, 48, 49, 46] followed the original non-interacting Fermi gas model of Hans Bethe [50]. For astrophysical nuclear reactions with temperature below a few times 10^{10} K [46, 51], this phenomenological approach gave excellent agreement with more sophisticated Monte Carlo shell model calculations [52], as well as combinatorial approaches [49, 53]. This justifies the application of the Fermi-gas description at and above the neutron separation energy. For temperatures higher than a few times 10^{10} K, there are big ambiguities in the values of the partition functions. However, as suggested by some authors [40] and supported by our own calculations, these uncertainties have only a small impact on the thermodynamics of dense matter.

The effects of Coulomb interactions in the plasma can be estimated by the plasma parameter $\Gamma_p = (Ze)^2/akT$, where Z is the atomic number of the nucleus, T is the temperature and a is the spacing between nuclei. For matter at low density, Γ_p is smaller than one and the effect of Coulomb corrections is small. However for matter at higher density and when the dominant species carry large charges, Γ_p can be much greater than one and the effect of Coulomb interactions should be taken into account. The Coulomb correction to the plasma has been studied analytically up to high Γ_p by the cluster expansion [54]. Generally the correction due to electron-ion interactions will reduce the free energy of the plasma and eventually crystalize the matter at high density. For simplicity, in this section the Coulomb interactions between nuclei and electrons are included via a Wigner-Seitz approximation with effective ion spheres for each species of nuclei, wherein local electrical neutrality is maintained. This WS approximation for the Coulomb correction will be compared with a more rigorous Cluster expansion method.

3.1. Average A and Z

The lower panels in Fig. 4 give the corresponding average charge number Z from the virial EoS with either FRDM or HFB14 mass tables [55], and from Hartree mean field results. Here temperature $T = 1$ (left panel) and 3.16 (right panel) MeV with proton fraction $Y_P = 0.3$. The virial EoS with the two mass tables predict very similar values for Z . Moreover, the virial EoS with either mass table gives very similar Z to that from the Hartree mean field results at the transition density $3.98 \times 10^{-3} \text{ fm}^{-3}$ (blue dotted line). One can also identify several plateaus in the average Z , which correspond to closed shells (magic numbers). The fluctuation of Z in Hartree results below the transition density (at $T = 3.16$ MeV) is probably due to finite step error in search of cell size. We also studied free energy and transition density to Hartree mean field results, and found little dependence on the choice of mass tables.

In the two upper panels in Fig. 4, we compare the Coulomb energy correction in our virial expansion, with an analytic cluster expansion for the one-component plasma, Eq. (22) in [54]. The overall agreement for densities below the virial-Hartree transition is good, though at higher temperature the differences become larger. The reason is probably that we calculate the multi-component contribution to the Coulomb correction in the virial gas while we only used the average charge number in the analytic formula for the one-component plasma.

3.2. Mass fractions of species

The virial expansion gives the distribution of heavy nuclei, where 8980 species of nuclei are in thermal and chemical equilibrium with free neutrons, free protons and alpha particles. This is an improvement over the L-S EoS and S-S EoS that both use a single-nucleus representation.

In Fig. 5 we show mass fractions of different nuclei for matter with $T = 1$ MeV, $Y_P = 0.4$, and $n_B = 10^{-3} \text{ fm}^{-3}$. The total mass fraction of heavy nuclei is close to unity and the distribution is centered around $Z = 35$ and 50. The mass distribution of heavy nuclei in this high Y_P case is a double-peaked Gaussian distribution, as shown in Fig. 6, where $n(Z)$ is sum of the abundances of heavy nuclei with same proton number Z .

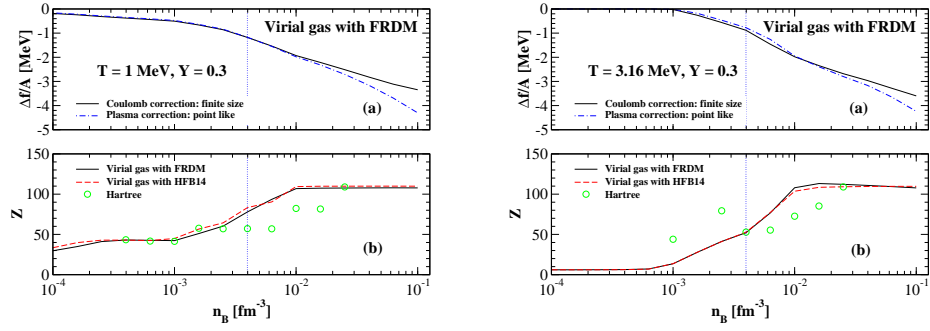


Figure 4. (color on line) Upper: Coulomb corrections; lower: average charge number of heavy nuclei, in nuclear matter at $T = 1$ (left panel) and 3.16 (right panel) MeV with $Y_P = 0.3$.

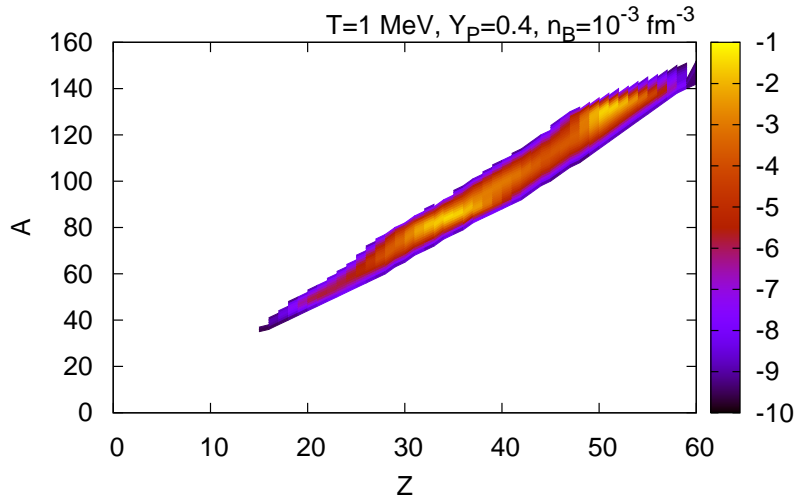


Figure 5. Mass fraction of nuclei in the nuclear chart for matter at $T = 1$ MeV, $n_B = 10^{-3}$ fm^{-3} , and $Y_P = 0.4$. Different colors indicate mass fraction in Log_{10} scale.

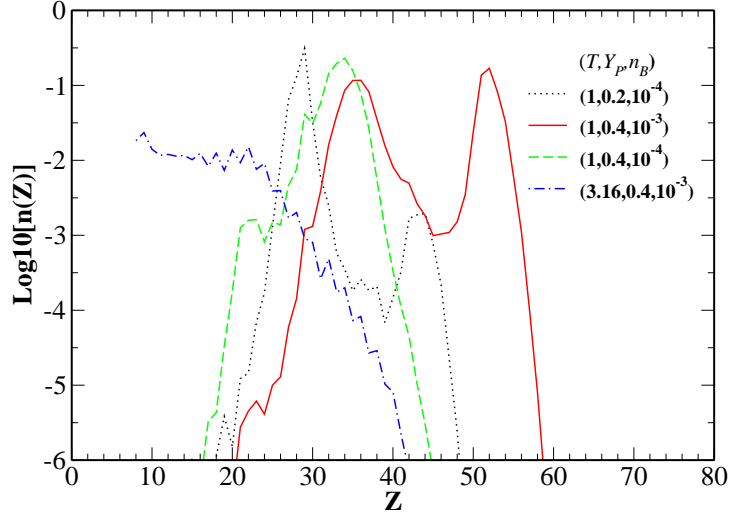


Figure 6. Mass fractions of nuclei $n(Z)$ for nuclei with same proton number Z . The triplet in the parenthesis stands for $(T/[\text{MeV}], Y_p, n_B/[\text{fm}^{-3}])$.

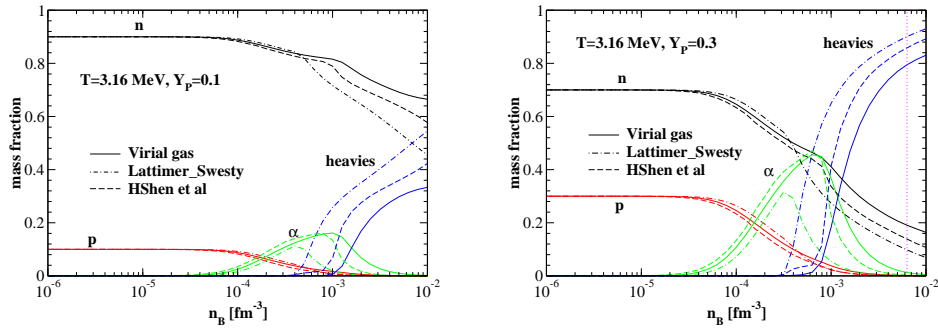


Figure 7. Mass fractions of matter at $T = 3.16$ (right) MeV, $Y_p = 0.1$ (left) or 0.3 (right) in our EoS (solid), Lattimer-Swesty EoS (dot-dashed) and H Shen *et al.* EoS (dashed).

It is instructive to compare the composition of matter in virial EoS with the existing EoS tables, the L-S EoS and S-S EoS. The location of neutrinosphere in supernova is sensitive to the composition of matter and is important for the emitted neutrino spectra. Studies on collective flavor oscillation of neutrinos during their streaming outside neutrinosphere have already indicated sensitivity of neutrino flavor flip to the emitted neutrino spectra in neutrinosphere [56]. Below we will compare some examples for the composition of matter around neutrinosphere from virial EoS, the L-S EoS, and S-S EoS.

Fig. 7 shows the mass fractions of neutrons, protons, alpha particles and nuclei in matter at densities from 10^{-6} to 10^{-2} fm^{-3} . The matter has a temperature of 3.16 MeV and a proton fraction of 0.1 (left) or 0.3 (right), respectively. In the left panel for proton fraction of 0.1, free neutrons and protons dominate until the density reaches 10^{-4} fm^{-3} in all three EoSs. Above 10^{-4} fm^{-3} , alpha particles appear. The S-S EoS is close to our virial results at densities roughly below 10^{-3} fm^{-3} . The L-S EoS significantly underestimate X_α and this may be due to an error in the alpha particle binding energy. Alpha particles have larger abundance and exists up to higher densities in our virial EoS than the other EoSs. This is partly because the attractive interactions between neutrons and alpha particles in the virial expansion favors more alpha particle [44]. Heavy nuclei begin to appear around $4 \cdot 10^{-4}$ fm^{-3} in the L-S EoS, and at higher densities in the S-S EoS and our virial EoS. Moreover, the L-S EoS predicts the largest abundance for heavy nuclei, while ours predicts the smallest abundance. Free neutrons have the largest abundance in our virial EoS. This is due to the strong attractive interaction between neutrons in the virial expansion which lowers the energy and enhances the abundance of neutrons. Note in this $Y_P = 0.1$ case the virial-Hartree transition happens at 0.0158 fm^{-3} . The right pane of Fig. 7, for a different proton fraction of 0.3, has similar characteristics. However here, alpha particles and heavy nuclei have much larger abundances than for the $Y_P = 0.1$ case, since a higher proton fraction favors formation of nuclei. In this $Y_P = 0.3$ case, the transition density from virial gas to Hartree mean field calculations occurs at $6.3 \cdot 10^{-3}$ fm^{-3} as indicated by the dotted line in the figure.

4. Complete EoS for PNS

In section 2 we used a relativistic mean field model to self-consistently calculate non-uniform matter at intermediate density and uniform matter at high density. In section 3 we used a Virial expansion for nonideal gas of nucleons and nuclei to obtain the EoS at low densities. Altogether these two EoS models cover the large range of temperatures, densities, and proton fractions. Discussion of matching the two results can be found in Ref. [57]. There are 73,840 data points from the Virial calculation at low densities, 17,021 data points from the nonuniform Hartree calculation, and 90,478 data points from uniform matter calculations. The overall calculations took 7,000 CPU days in Indiana University's supercomputer clusters.

In Fig. 8, we show the phase boundaries of nuclear matter at different proton fractions $Y_P = 0.05, 0.1, 0.2$ and 0.4 . The mass fraction of heavy nuclei with mass number $A > 4$ is X_A . The boundary at low densities indicates when X_A is greater or less than 10^{-3} . The boundary at high densities indicates the transition between non-uniform matter and uniform matter. At very low densities, the matter is dominated by free nucleons and alpha

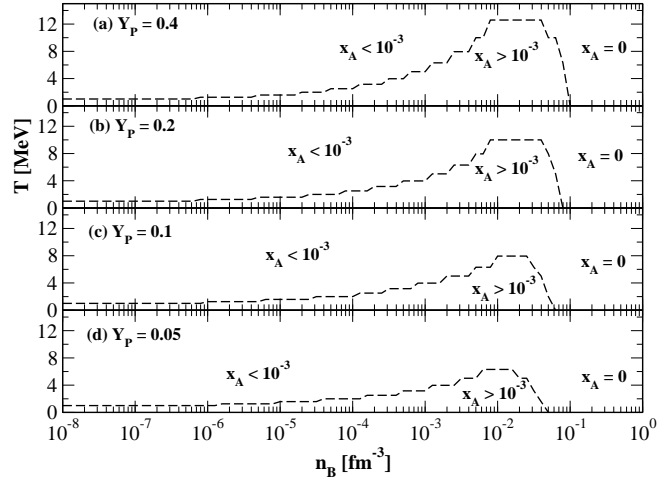


Figure 8. Phase diagram of nuclear matter at different proton fractions, 0.05, 0.1, 0.2 and 0.4. X_A is mass fraction of heavy nuclei with mass number $A > 4$.

particles. As the density rises, heavy nuclei persist to higher temperatures. Finally uniform matter takes over at sufficiently high density. Figure 8 also shows that as the proton fraction rises, the temperature regime with appreciable heavy nuclei grows and the transition density to uniform matter increases. The density for the nonuniform matter to uniform matter transition has a weak temperature dependence.

We use a hybrid interpolation scheme to generate a full EoS table on a fine grid that is thermodynamically consistent. The range of parameter spaces is shown in Table 1. This insures that the first law of thermodynamics is satisfied and that entropy is conserved during adiabatic compression. Our EoS is an improvement over the existing Lattimer-Swesty [17] and H. Shen *et al.* [18, 43], equations of state because our EoS includes thousands of heavy nuclei and is exact in the low density limit.

We also generated a second EoS based on the RMF effective interaction FSUGold [58, 59], whereas our earlier EoS was based on the RMF effective interaction NL3. The FSUGold interaction has a lower pressure at high densities compared to the NL3 interaction. The original FSUGold interaction produces an EoS, that we call FSU1.7, that has a maximum neutron star mass of 1.7 solar masses. A modification in the high density EoS is introduced to increase the maximum neutron star mass to 2.1 solar masses and results in a slightly different EoS that we call FSU2.1. Finally, the EoS tables for NL3, FSU1.7 and FSU2.1 are available for download.

5. Symmetry Energy in Various EoS

The bulk properties of infinite nuclear matter have been collected in Table 2, for NL3, FSUGold, as well as a new effective RMF interaction IUFSU [60]. One important dis-

Table 1. Range of temperature T , density n_B , and proton fraction Y_p in the finely spaced interpolated EoS table.

| Parameter | minimum | maximum | number of points |
|---------------------------------------|----------------|--------------|------------------|
| T [MeV] | 0, $10^{-0.8}$ | $10^{1.875}$ | 109 |
| $\log_{10}(n_B)$ [fm^{-3}] | -8.0 | 0.175 | 328 |
| Y_P | 0, 0.05 | 0.56 | $1(Y_P=0)+52$ |

| Model | ρ_0 (fm^{-3}) | ε_0 (MeV) | K_0 (MeV) | E_{sym} (MeV) | L (MeV) |
|--------|-------------------------------|-----------------------|-------------|-----------------|-----------|
| NL3 | 0.148 | -16.24 | 271.5 | 37.29 | 118.2 |
| FSU | 0.148 | -16.30 | 230.0 | 32.59 | 60.5 |
| IU-FSU | 0.155 | -16.40 | 231.2 | 31.30 | 47.2 |

Table 2. Bulk parameters characterizing the behavior of infinite nuclear matter at saturation density ρ_0 . The quantities ε_0 and K_0 represent the binding energy per nucleon and incompressibility coefficient of symmetric nuclear matter, whereas E_{sym} and L represent the energy and slope of the symmetry energy at saturation density.

tion among various EoS is the slope of the symmetry energy at saturation density, $L/3 = \rho_0 E'_{sym}(\rho_0)$. The pressure around saturation density is proportional to L , which plays a crucial role both in the terrestrial context where it affects the neutron density distribution in neutron rich nuclei and in astrophysics where it affects the structure and thermal evolution of neutron stars.

Brown first realized the correlation between L and the neutron skin thickness of ^{208}Pb [3], which has 126 neutrons and 82 protons. A larger pressure - due to larger L inside the nucleus will push neutrons to the surface, therefore leads to a bigger neutron skin thickness. This is clearly demonstrated in left panel of Fig. 9, where the proton and neutron densities inside ^{208}Pb are shown from several model predictions. The proton density is well constrained to 1%. In contrast the neutron density has sizable variations among different model predictions. The values of L are 118.2, 60.5, and 47.2 MeV for NL3, FSU, and IUFSU, respectively. The resulting neutron skin thickness is 0.28, 0.21, and 0.16 fm for NL3, FSU, and IUFSU, respectively. The pressure of neutron matter around saturation density also influences the radius of cold neutron star [6, 61]. In the right panel of Fig. 9, we show the neutron star mass-radius relation for various RMF models. For 1.4 solar mass neutron star, the corresponding radii are 15, 12.8, and 12.5 km for NL3, FSU, and IUFSU, respectively. FUS2.1 has a larger pressure than FSU1.7 at density above 0.2 fm^{-3} , and gives rise to larger radius for 1.4 solar mass neutron star, 13.6 km. Due to their common relation to the derivative of symmetry energy L , there exists a correlation between the neutron skin thickness and neutron star radius [6].

It's our goal to calculate EoS tables with different pressures. This will allow one to correlate features of astrophysical simulations with EoS properties. In this work we discussed two new EoS based on different RMF effective interactions NL3 and FSUGold. In future we will present a third EoS based on IU-FSU like effective interaction which has a softer symmetry energy L .

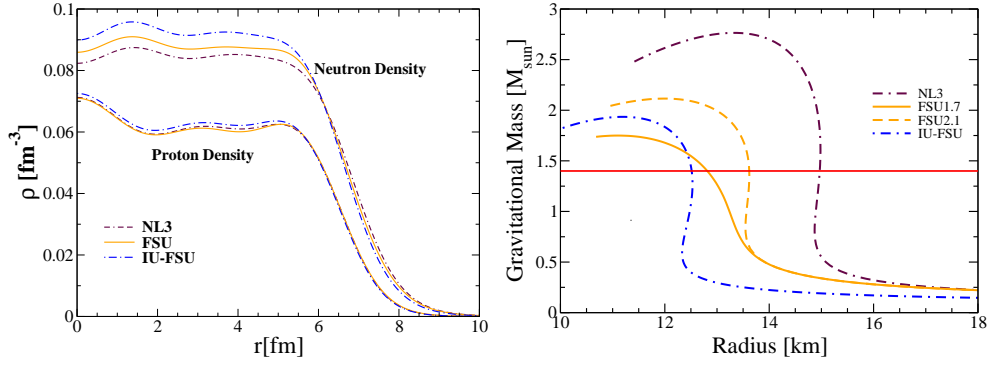


Figure 9. (Color online) Left: model predictions for the proton and neutron densities of ^{208}Pb . Right: Neutron Star *Mass-vs-Radius* relation predicted by the relativistic mean-field models discussed in the text.

6. Conclusions

Equation of state of nuclear matter at finite temperature and its dynamics is the key to understand the evolution of proto-neutron star. The pressure at high densities determines how big and large a neutron star nature could make. The composition of matter in PNS and its dynamical response with neutrinos is important for the evolution of PNS. The emergent neutrino spectra from neutrino-sphere is crucial for the neutron fraction in the neutrino-driven wind and possible r-process that could make heavy nuclei beyond iron. The EoS of nuclear matter has been the focus of heavy ion collision experiments and a future heavy ion accelerator FRIB.

We construct several new EoS of nuclear matter for a wide range of temperatures, densities, and proton fractions. We employ fully microscopic relativistic mean field calculation for matter at intermediate density and high density, and the virial expansion of a nonideal gas (with nucleons and 8981 kinds of nuclei) for matter at low density. The EoS was obtained at over 180,000 grid points in 3-dimensional parameter spaces (temperature, density, and proton fraction). We used hybrid interpolation scheme to generate the final table, as shown in Table 1. The thermodynamic consistency in our table is checked via usual adiabatic compression test, where the oscillation in entropy is limited to 1% using the finer table Ref. [57, 59].

For nonuniform matter we find new shell states which minimize the free energy per baryon over a significant density range. Shell states have inside and outside surfaces and they can minimize the Coulomb energy of high Z (large proton number) configurations at the expense of a larger surface energy. The appearance of shell states may significantly change transport properties such as the shear viscosity and shear modulus of neutron rich matter. The virial expansion gave broad distributions of nuclei in the nuclear chart, that are absent in two commonly used EOS tables, the Lattimer-Swesty EOS and H. Shen *et al.* EOS. These distributions of nuclei may be important for neutrino-matter interactions in supernova and the position of neutrino-sphere in supernova. The virial gas reduces to nuclear statistical equilibrium at low density and is exact in low density limit. Our new

table is an improvement over existing EOS tables. We aim to provide detailed composition information in future EoS tables. This can be important for neutrino interactions.

Due to the rather large uncertainties in the EoS at high density, particularly the density dependence of symmetry energy, we generated two EoS tables based on a stiff EoS at high density, NL3, and a softer EoS at low density, FSU1.7, and the modified FSU2.1 which could support a 2.1 solar mass neutron star. In future we will generate a third EoS based on IU-FSU like interaction, which is soft around saturation density but stiff at higher densities. Altogether these EoS tables could cover the uncertainties in the properties of nuclear matter at high density, and astrophysical simulations with them could identify observational phenomena with distinct nuclear matter property.

The property of neutron rich matter has yet to be fully understood, and currently under extensive studies both in experiments, such as PREX to measure the neutron skin thickness of ^{208}Pb , and in theory, such as chiral effective theory calculation to third order perturbative expansion [62] and quantum Monte Carlo method with uncertain 3-body forces [63]. There are also important efforts to determine the EoS based on statistical analysis on the observational data such as X-ray burst on neutron stars [64, 65].

Probably an equally important problem for the PNS is the dynamical response of nuclear matter. Nuclear pasta could dominate in the composition of inner crust and neutrinos could scatter coherently on them [8, 66]. Dynamical response of nuclear matter around neutrinosphere where light nuclei abound is important for the emitted neutrino spectra [9]. All these neutrino interactions have yet to be included in the studies of PNS evolution.

The author acknowledges supports by a grant from the DOE under contract DE-AC52-06NA25396 and the DOE topical collaboration to study "Neutrinos and nucleosynthesis in hot and dense matter" during write-up of this work.

References

- [1] Ch. Hartnack, H. Oeschler, and Jörg Aichelin, Phys. Rev. Lett. **96**, 012302 (2006). P. Danielewicz, R. Lacey, and W. G. Lynch, Science **22**, 1592 (2002).
- [2] Facility for Rare Isotope Beams project, <http://www.frib.msu.edu>.
- [3] B. A. Brown, Phys. Rev. Lett. **85**, 5296 (2000) .
- [4] Jefferson Laboratory Experiment E-06-002, Spokespersons K. Kumar, R. Michaels, P. A. Souder, and G. M. Urciuoli.
- [5] C. J. Horowitz, S. J. Pollock, P. A. Souder, and R. Michaels, Phys. Rev. C **63**, 025501 (2001).
- [6] C. J. Horowitz and J. Piekarewicz, Phys. Rev. Lett. **86**, 5647 (2001).
- [7] H. Sonoda, G. Watanabe, K.Sato, K. Yasuoka, and T. Ebisuzaki, Phys. Rev. C **77**, 035806 (2008).
- [8] C. J. Horowitz, M. A. Pérez-García, J. Carriere, D. K. Berry, and J. Piekarewicz, Phys. Rev. C **70**, 065806 (2004).

-
- [9] A. Arcones, G. Martínez-Pinedo, E. O'Connor, A. Schwenk, H.-T. Janka, C. J. Horowitz, and K. Langanke, *Phys. Rev. C* **78**, 015806 (2008).
- [10] See for example, Huaiyu Duan, Alexander Friedland, Gail C. McLaughlin, and Rebecca Surman, *J. Phys. G: Nucl. Part. Phys.* **38**, 035201 (2011).
- [11] J. W. Negele and D. Vautherin, *Nucl. Phys. A* **207**, 298 (1973).
- [12] See for example T. Maruyama, T. Tatsumi, D. N. Voskresensky, T. Tanigawa, and S. Chiba, *Phys. Rev. C* **72**, 015802 (2005).
- [13] D. G. Ravenhall, C. J. Pethick, and J. R. Wilson, *Phys. Rev. Lett.* **50**, 2066 (1983).
- [14] C. P. Lorenz, D. G. Ravenhall, and C. J. Pethick, *Phys. Rev. Lett.* **70**, 379 (1993).
- [15] C. J. Horowitz, M. A. Pérez-García, and J. Piekarewicz, *Phys. Rev. C* **69**, 045804 (2004).
- [16] C. J. Jog and R. A. Smith, *Astrophys. J.* **253**, 839 (1982).
- [17] J. M. Lattimer and F. D. Swesty, *Nucl. Phys. A* **535**, 331 (1991).
- [18] H. Shen, H. Toki, K. Oyamatsu, and K. Sumiyoshi, *Nucl. Phys. A* **637**, 435 (1998).
- [19] C. J. Horowitz and B. D. Serot, *Nucl. Phys. A* **368**, 503 (1981).
- [20] B. D. Serot, *Phys. Lett. B* **86**, 146 (1979).
- [21] B. D. Serot and J. D. Walecka, *Adv. Nucl. Phys.* **16**, 1 (1986).
- [22] P.-G. Reinhard, *Rep. Prog. Phys.* **52**, 439 (1989).
- [23] P. Ring, *Prog. Part. Nucl. Phys.* **37**, 193 (1996).
- [24] G. Shen, C. J. Horowitz, and S. Teige, *Phys. Rev. C* **82**, 015806 (2010).
- [25] C. J. Horowitz and G. Shen, *Phys. Rev. C* **78**, 015801 (2008).
- [26] C. J. Horowitz and A. Schwenk, *Phys. Lett. B* **638**, 153 (2006).
- [27] G. A. Lalazissis, J. König, and P. Ring, *Phys. Rev. C* **55**, 540 (1997).
- [28] C. J. Horowitz and G. Shen, *Phys. Rev. C* **78**, 015801 (2008).
- [29] See for example P. Gögelein, E. N. E. van Dalen, C. Fuchs, and H. Mütter, *Phys. Rev. C* **77**, 025802 (2008).
- [30] G. Shen, C. J. Horowitz and S. Teige, *Phys. Rev. C* **82**, 045802 (2010).
- [31] C. Kittel, *Introduction to Solid State Physics*, P. 571, John Wiley & Sons Inc, 2nd Edition (1956).
- [32] K. Oyamatsu, M. Hashimoto, and M. Yamada, *Prog. Theor. Phys.* **72**, 373 (1984).

-
- [33] C. J. Pethick and D. G. Ravenhall, *Ann. Rev. Nucl. Part. Sci.* **45**, 429 (1995).
- [34] P. Haensel, A. Y. Potekhin, and D. G. Yakovlev, *Neutron Stars 1: Equation of State and Structure*, *Astrophysics and Space Science Library*, vol. 326, (Springer, New York, U.S.A., 2007).
- [35] A. V. Afanasjev and S. Frauendorf, *Phys. Rev. C* **71**, 024308 (2005).
- [36] A. Burrows, S. Reddy, and T. A. Thompson, *Nucl. Phys. A* **777**, 356 (2006).
- [37] M. Costantini, A. Ianni, and F. Visanni, *Phys. Rev. D* **70**, 043006 (2004).
- [38] C. Lunardini and A. Y. Smirnov, *Astropart. Phys.* **21**, 703 (2004).
- [39] B. S. Meyer, *Ann. Rev. Astron. Astrophys.* **32**, 153 (1994).
- [40] S. I. Blinnikov, I. V. Panov, M. A. Rudzsky, and K. Sumiyoshi, arXiv: 0904.3849.
- [41] M. Hempel and J. Schaffner-Bielich, *Nucl. Phys. A* **837**, 210 (2010).
- [42] P. Möller, J. R. Nix, and W. J. Swiatecki, *Atom. Data Nucl. Data Tables*, **59**, 185 (1995).
- [43] H. Shen, H. Toki, K. Oyamatsu, and K. Sumiyoshi, *Prog. Theo. Phys.* **100**, 1013 (1998).
- [44] C. J. Horowitz and A. Schwenk, *Nucl. Phys. A* **776**, 55 (2006).
- [45] W. A. Fowler, C. A. Engelbrecht, and S. E. Woosley, *ApJ* **226**, 984 (1978).
- [46] T. Rauscher, F.-K. Thielemann, and K.-L. Kratz, *Phys. Rev. C* **56**, 1613 (1997).
- [47] A. Gilbert and A. G. W. Cameron, *Canadian Journal of Physics.* **43**, 1446 (1965).
- [48] T. J. Mazurek, J. M. Lattimer, and G. E. Brown, *ApJ* **229**, 713 (1979).
- [49] C. A. Engelbrecht and J. R. Engelbrecht, *Ann. Phys.* **207**, 1 (1991).
- [50] H. A. Bethe, *Phys. Rev.* **50**, 332 (1936).
- [51] T. Rauscher and F.-K. Thielemann, *Atom. Data Nucl. Data Tab.* **75**, 1 (2000).
- [52] D. J. Dean, S. E. Koonin, K.-H. Langanke, P. B. Radha, and Y. Alhassid, *Phys. Rev. Lett.* **74**, 2909 (1995).
- [53] V. Paar and R. Pezer, *Phys. Rev. C* **55**, R1637 (1997).
- [54] N. V. Brilliantov, *Contrib. Plasma Phys.* **38**, N4 (1998).
- [55] S. Goriely, M. Samyn, and J. M. Pearson, *Phys. Rev. C* **75**, 064312 (2007).
- [56] See for a recent review, H. Duan, G. M. Fuller, and Y.-Z. Qian, *Ann. Rev. Nucl. Part. Sci.* **60**, 569 (2010).

- [57] G. Shen, C. J. Horowitz, and S. Teige, *Phys. Rev. C* **83**, 035802 (2011).
- [58] B. G. Todd-Rutel and J. Piekarewicz, *Phys. Rev. Lett.* **95**, 122501 (2005).
- [59] G. Shen, C. J. Horowitz, and E. O'Connor, *Phys. Rev. C* **83**, 065808 (2011).
- [60] F. J. Fattoyev, C. J. Horowitz, J. Piekarewicz, and G. Shen, *Phys. Rev. C* **82**, 055803 (2010).
- [61] J. M. Lattimer and M. Prakash, *Astrophys. J.* **550**, 426 (2001).
- [62] K. Hebeler, J.M. Lattimer, C.J. Pethick, and A. Schwenk, *Phys. Rev. Lett.* **105**, 161102 (2010).
- [63] S. Gandolfi, J. Carlson, and Sanjay Reddy, arXiv:1101.1921.
- [64] F. Özel, G. Baym, and T. Guver, *Phys. Rev. D* **82**, 101301 (2010).
- [65] Andrew W. Steiner, James M. Lattimer and Edward F. Brown, *Astrophys. J.* **722**, 33 (2010).
- [66] H. Sonoda, G. Wanatabe, K. Sato, T. Takiwaki, K. Yasuoka, and T. Ebisuzaki, *Phys. Rev. C* **75**, 042801 (2007).